Scripta Materialia 203 (2021) 114092

Contents lists available at ScienceDirect

Scripta Materialia

journal homepage: www.elsevier.com/locate/scriptamat

An innovative way to fabricate γ-TiAl blades and their failure mechanisms under thermal shock

R. Gao[a], H. Peng[b,*], H. Guo[b], B. Chen[c,*]

[a] School of Materials Science and Engineering, Beihang University, Beijing 100191, China
[b] Key Laboratory of High-Temperature Structural Materials & Coatings Technology, Ministry of Industry and Information Technology, Beihang University, 37 Xueyuan Road, Beijing 100191, China
[c] School of Engineering, University of Leicester, Leicester, LE1 7RH, UK

ARTICLE INFO

Article history:
Received 14 April 2021
Revised 9 June 2021
Accepted 13 June 2021
Available online 23 June 2021

Keywords:
Titanium aluminides
Intermetallic compounds
Selective electron beam melting
Additive manufacturing
Thermal shock

ABSTRACT

The near-net-shape γ-TiAl blades were built by selective electron beam melting. As-fabricated material exhibits a good combination of microstructure homogeneity, tensile properties and thermal shock resistance at 700 °C owing to the optimised process parameters. The consistent and reliable approach to achieve this manufacturing success is elaborated. By performing thermal shock experiments at 900 °C, a new cracking mechanism has been identified. Through the post-mortem examinations, we reveal that such failure mode is most likely associated with the layer-by-layer strategy. Oxidation in conjunction with the surface topology is the underlying mechanism.

Strong interest in γ-TiAl traces back to 1980s, and this lightweight intermetallic alloy, as a replacement for the heavier Ni-base superalloy, has been used for manufacturing low-pressure turbine blades [1]. The γ-TiAl alloy consisting of multi-phases (fcc γ-TiAl, hcp α_2-Ti_3Al, and bcc β/B2) is manufactured by casting or powder metallurgy, followed by thermo-mechanical processing and/or heat treatments to obtain desired microstructures. However, its wider industrial adoption is limited by the chemical and microstructure inhomogeneity, manufacturing difficulties and high costs, causing large scatter in properties. Microstructure refinement is one way to obtain well balanced and reproducible properties [2].

Recent years have seen a tremendous increase in publications about γ-TiAl alloys processed by selective electron beam melting (SEBM), a powder-bed fusion additive manufacturing. Following the pioneering work on SEBM γ-TiAl by Cormier et al. [3], many researchers have advanced this field including, but not limited to, Murr et al. [4], Schwerdtfeger and Korner [5], Biamino et al. [6], Todai et al. [7] and Kan et al. [8]. Despite the success in SEBM γ-TiAl bulk samples, little work has been performed towards the near-net-shape blade.

Here we report on the SEBM processing of Ti-48Al-2Cr-2Nb alloy blades. We show excellent high-temperature tensile properties and thermal shock resistance at 700 °C. We reveal oxidation induced cracking in thermal shock experiment at 900 °C, and the underlying mechanism is elucidated.

Gas-atomised Ti-48Al-2Cr-2Nb powder with average particle size of 87.5 μm was used for SEBM processing. Particle size distribution was determined as 42.5, 81.3 and 142.0 μm for D_{10}, D_{50} and D_{90} by laser particle diffraction (Fig. 1a). The powder has a spherical shape (inset of Fig. 1a), exhibiting a good flowability (24.5 s) and apparent density (2.3 g/cm^3). The chemical composition was determined as Ti-48.6Al-1.97Cr-1.98Nb (all in at.%, measured by ICP-AES).

Arcam A2XX machine was used to fabricate the γ-TiAl blades as well as sample coupons with dimensions of 10 × 10 × 70 mm^3, Fig. 1b. Contour melt was on, snake-like path was off, and 90° scan rotation was applied between layers. The height of the blade was measured as 70 mm along the radial direction. The distance between leading and trailing edges within the aerofoil portion was 16.6 mm. They were built layer-by-layer on the top of a stainless-steel starting plate (Φ155 × 20 mm), with a layer thickness of 90 μm. A thermocouple was attached to the bottom of the plate to measure the build temperature. The whole fabrication was performed under a vacuum pressure of 1 × 10^{-2} mbar with high-purity helium used as regulating gas.

Process stability is key to ensuring the integrity of SEBM alloys [9,10]. To avoid the smoke phenomenon, a powder pre-sinter step was employed by using a focus offset of 40 mA, average current

* Corresponding authors.
E-mail addresses: penghui@buaa.edu.cn (H. Peng), bo.chen@leicester.ac.uk (B. Chen).

https://doi.org/10.1016/j.scriptamat.2021.114092

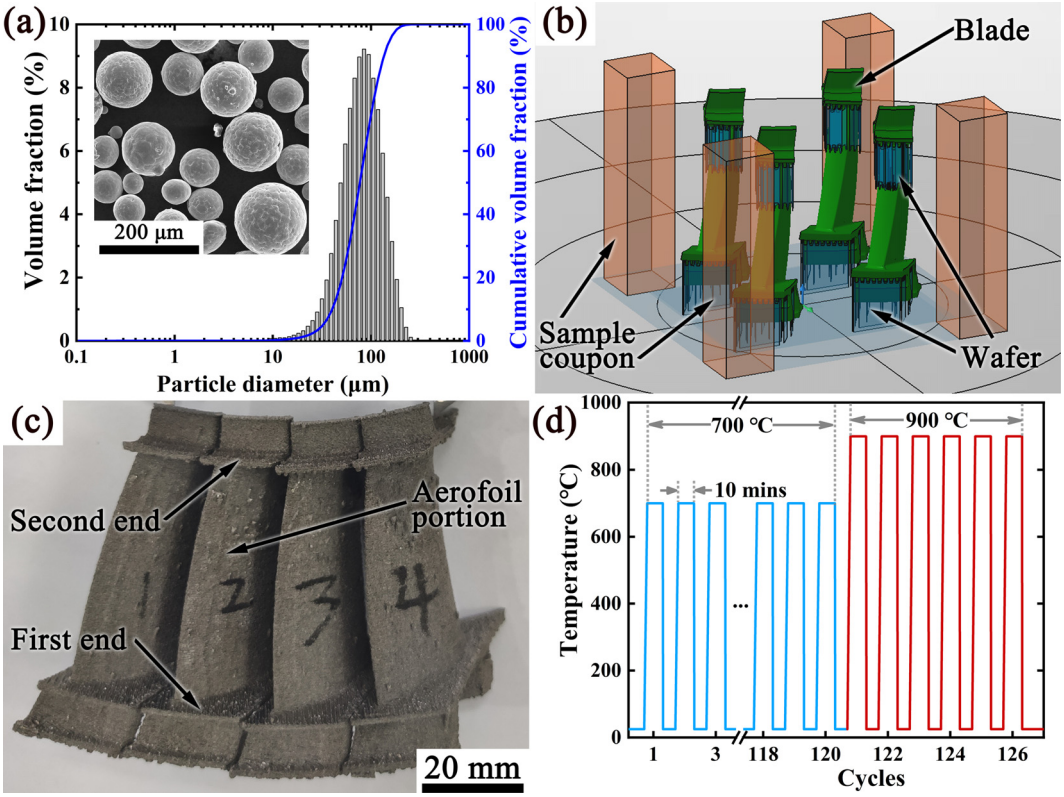

Fig. 1. SEBM γ-TiAl blades and sample coupons produced in the same batch: (a) Ti-48Al-2Cr-2Nb powder characteristics; (b) CAD model illustrating locations of the blades, wafers and sample coupons on the starting plate; (c) photo showing the as-fabricated blades; (d) temperature profile in thermal shock experiments.

Table 1
Process parameters during different steps in SEBM.

Steps	Beam, mA		Scan strategy		
	Focus offset	Maximum current	Average current	Scan speed, mm/s	Line offset, mm
Pre-sinter	40	20	5	10000	0.3
Preheat 1	150	35	28	10000	1
Preheat 2	150	45	30	10000	1
Melt	0	20	\	Function 55	0.2
Wafer	0	4	4	650	\

of 5 mA, and line offset of 0.3 mm (Table 1). The pre-sinter step was followed by pre-heat 1 and 2 using the parameters listed in Table 1. Pre-heat 1 helped to maintain the powder-bed temperature on an area of 130 mm in diameter, while pre-heat 2 was given to the regions near the parts to achieve the build temperature of 1030 °C. We observed no smoke during the subsequent melt step.

In terms of the melt step, two interconnected beam parameters deserve particular attention while printing the part in auto mode: scan speed and beam current. The speed function technology [11] was used to adjust their values, depending on the length of specific scanline, maximum beam current, reference length and the proportionality. Speed function 55 together with the maximum current of 20 mA and line offset of 0.2 mm was employed, Table 1. Refer to Fig. S1a and the accompanying text for more details.

The average beam current is not specified in Table 1 because its value is determined by the melt area and build height (Fig. S1b). The average current increases with the build height to compensate the energy loss through the conduction. Also, its value increases with the melt area to offset the energy loss due to radiation. A tilt angle of 18° between the radial direction of the blade and the Z-build direction was applied to help reduce the abrupt change of beam current at the moment of printing the first and second ends (Fig. 1b). The sudden change would increase the likelihood of creating defects (e.g. lack-of-fusion [12]) and microstructure inhomogeneity [13]. Furthermore, wafer supports (parameters given in Table 1) were prepared at locations where the two ends were processed to reduce the thermal stress induced deformation. The as-fabricated γ-TiAl blades with no visible surface crack is shown in Fig. 1c.

Uniaxial tensile tests at 700 °C were performed under constant rate of 0.2 mm/min using specimens (gauge length of 15 mm and diameter of 3 mm) extracted from the centre of SEBM sample coupons with their tensile axis parallel to the build direction. Fractographic examination was performed using a JEOL-6010 scanning electron microscope (SEM). To examine the microstructure inhomogeneity and porosity, cross-sections were made perpendicular to the radial direction of the blade at different Z-heights with three of them within the aerofoil portion and one at the outer platform. Samples were polished down to 0.5 μm for quantitative examination using optical (Leica DM4000) and electron microscopy (Zeiss Gemini-300 FEG-SEM equipped with EDS detector) as well as the micro-hardness tester. Tranmission electron microscopy (TEM, JEOL 2100) was conducted to characterise the lamellar structure.

Thermal shock experiment was conducted at 700 °C in accordance with the service temperature [14]. The blade was heated in a furnace for 10 mins followed by free fall into a water bath, and this

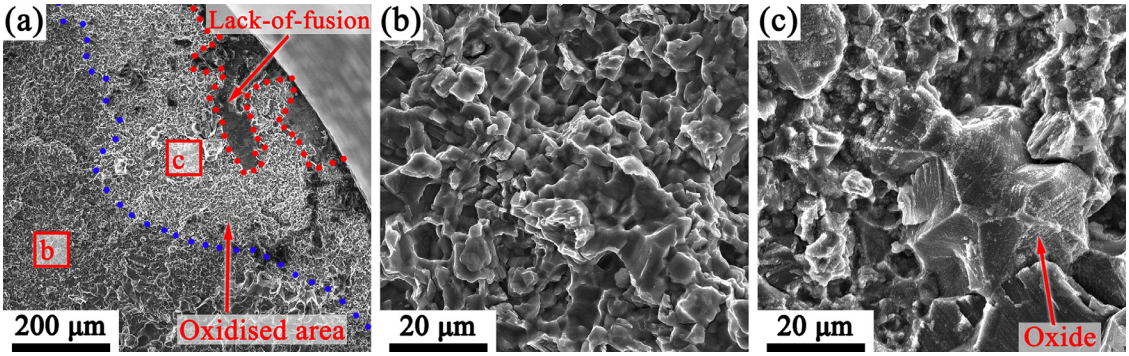

Fig. 2. SEM fractography: (a) crack initiation site showing lack-of-fusion defect and oxidised area; (b) enlarged view showing the non-oxidised fracture surface; (c) enlarged view of the oxidised area.

procedure was repeated for 120 cycles, see blue lines in Fig. 1d. No surface crack was revealed. We then raised the thermal-shock temperature to 900 °C (target temperature for the next generation of γ-TiAl [15–17]). Cracks perpendicular to the radial direction appeared at the surface of the aerofoil portion after 6 cycles (Fig. 1d). Thus, the thermal-shock experiment was terminated.

The yield strength, ultimate tensile strength and elongation-to-fracture at 700 °C were measured as 487.7±3.3, 512.3±7.3 and 1.31±0.24 % (the average of three tests, Table S1). The tensile property of SEBM γ-TiAl sample coupons, fractured in a transgranular manner [18], is as good as that reported previously [6,7]. SEM fractography revealed that the fatal-crack initiated from a lack-of-fusion defect near the surface (Fig. S2). The enlarged SEM view in Fig. 2a clearly identified two distinct regions with (Fig. 2c) and without (Fig. 2b) surface oxides. It seems that the crack, initiated from the defect, grew steadily before triggering the final fracture. The presence of discontinuous oxide particles (Fig. 2c) suggests that oxidation most likely occurred after the crack initiation.

The SEBM γ-TiAl blade exhibited a duplex microstructure with the γ/α_2 lamellar colony and equiaxed γ for both the aerofoil portion and outer platform (Fig. 3a and 3c). The B2-phase containing high Nb appeared with the brighter contrast under SEM (Fig. S3 for phase identification). The porosity level was determined as 0.26% based on metallography, and the relative density was 99.2±0.2% (Archimedes drainage method); both indicate good process stability. Little difference was found between the two regions.

The TEM thin foils prepared from the aerofoil portion was oriented with the $\langle 1\bar{1}0]_\gamma \| \langle 11\bar{2}0\rangle_{\alpha 2}$ zone axis in edge-on condition to minimise overlapping of lamellae. The selected area diffraction patterns (SADPs) in Fig. 3f confirmed their identity. The ultra-fine lamellar structure, Fig. 3d, was characterised by the lamellar spacing of $\lambda_{\alpha 2}$=13.3±6.7 nm and λ_γ=36.9±19.6 nm. Their sizes are one order of magnitude smaller than those in the cast γ-TiAl [19]. However, the coarser lamellar structure with $\lambda_{\alpha 2}$=210.6±82.5 nm and λ_γ=621.7±285.7 nm, Fig. 3e, suggests that the discontinuous coarsening occurred during the SEBM process [20], given that the lamellar structure becomes unstable at elevated temperature [21]. TEM also confirmed the nature of equiaxed γ- and B2-phases (Fig. S3c to S3f). The measured $(100)_{B2}$ and $(101)_{B2}$ interplanar spacings (d_{100}=3.33 Å and d_{101}=2.36 Å, Fig. S3f) agreed reasonably well with the literature [22]. The presence of B2-phase can be attributed to the high cooling rate and Al loss related to the SEBM process. The former inhibits the nucleation of the α-phase [23], while the latter expands the single β-phase region at high temperature [8].

To quantitatively assess the spatial gradient along the Z-build direction and within the aerofoil, three cross-sections perpendicular to the radial direction were prepared at Z=23, 36 and 51 mm (Fig. 3b). The lamellar colony size and volume fraction were measured as 9.7±6.0 μm and 66.3±3.2% at Z=23 mm, 8.3±4.5 μm and 63.7±2.6% at Z=36 mm, and 9.0±5.4 μm and 59.9±3.5% at Z=51 mm, respectively (Fig. S4). Thus, there was insignificant gradient along the Z-build, being consistent with the Al loss (3.11±0.17%, 3.52±0.15% and 4.36±0.18%, Fig. S5). The average micro-hardness was measured as 279.7±6.5 and 302.3±8.3 $HV_{0.5}$ across a distance of 4 mm, indicating a relatively low scatter (Fig. S4b). Note that a different microstructure was found close to the trailing and leading edges, probably due to the contour melt [24]. Overall, the as-built γ-TiAl blade exhibits a good combination of microstructure homogeneity, tensile properties and thermal shock resistance at 700 °C.

After raising the temperature to 900 °C (Fig. 1d), 6 thermal-shock cycles led to surface cracking as observed from the suction side of the aerofoil, Fig. 4a. Main cracks were found perpendicular to the radial direction of the blade. The cracked surface was opened up to allow examining the fracture surface under SEM. It is evident that crack initiation occurred from the suction side near the trailing edge, Fig. 4b. Meanwhile, the layerwise AM fabrication traces can be seen at the suction side, suggesting that there might be some correlation between the surface topology induced oxidation and the crack initiation under thermal shock. Fig. 4c is the enlarged view of the rectangular box in Fig. 4b, highlighting the presence of continuous oxide scales (16.2 μm in thickness) on the fractured surface, with the observed cracks indicating their brittle nature.

To further substantiate the oxidation associated crack mechanism, the crack path was studied via the metallographic cross-section, Fig. 4a. The crack shown in Fig. 5a represents a typical one at the middle position of the suction side having the total crack length of 9.9 mm, while the one with the total length of 466.7 μm (Fig. S6) was found near the trailing edge. No difference was found between the two cases, and all surface-crack initiations were exclusively associated with the traces of the layerwise AM fabrication. The crack seemed to initiate from the valley on the blade surface (Fig. 5a and Fig. S6a), which was the same location for connecting the two adjacent layers, given that the powders adhering to the surface are visible near the valley (Fig. 5e).

Fig. 5b is the enlarged view of Fig. 5a, where EDS mapping of Al, Ti, Nb and O was collected. The absence of Nb enrichment was confirmed along the crack path, Fig. 5g (the same for Cr). The O enrichment appeared along the crack path until the crack deflection occurred, Fig. 5f. The BSE SEM image (Fig. 5b) revealed a distinct phase contrast between the two regions with the latter appeared as greyish. This can be attributed to the preferential formation of alumina as opposed to Ti-oxides for TiAl alloys [25–27]. Prior to the oxide formation, the region close to the crack is thus expected to show Al depletion; this is exactly what was observed in Fig. 5d.

To elucidate the oxidation mechanism, a high-magnification EDS mapping was performed together with the point analyses (Fig.

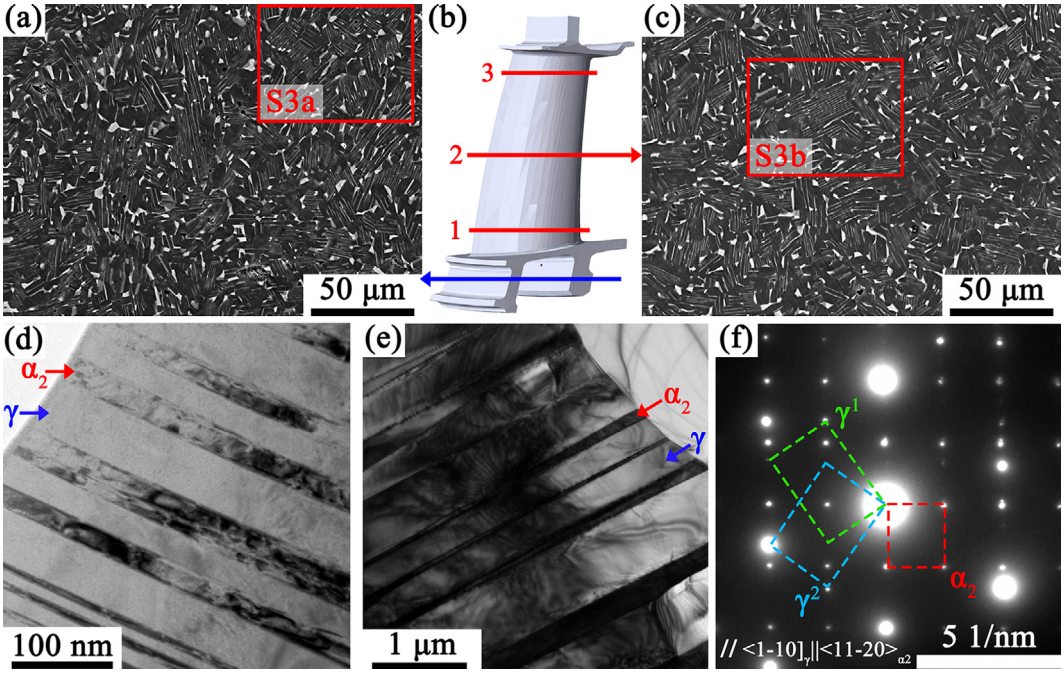

Fig. 3. Representative microstructures as observed in the outer platform in (a) and aerofoil portion in (c) to (f) of the SEBM-processed γ-TiAl blade as schematically shown in (b): (a) SEM micrograph showing microstructure in the outer platform; (c) SEM micrograph from the aerofoil portion; (d) TEM bright-field image showing the nanoscale lamellar microstructure; (e) TEM bright-field image showing the coarser lamellar microstructure; (f) TEM SADPs showing the α_2 and γ variants coexisting within a single lamellar colony with shared zone axes of $<1\text{-}10]_\gamma||<11\text{-}20>_{\alpha 2}$, referring to Fig. S3g and S3h for the indexed α_2 and γ diffraction spots. Note: additional SEM and TEM micrographs can be found in Fig. S3 and S4, while the measured Al loss in Fig. S5 for the quantitative evaluation.

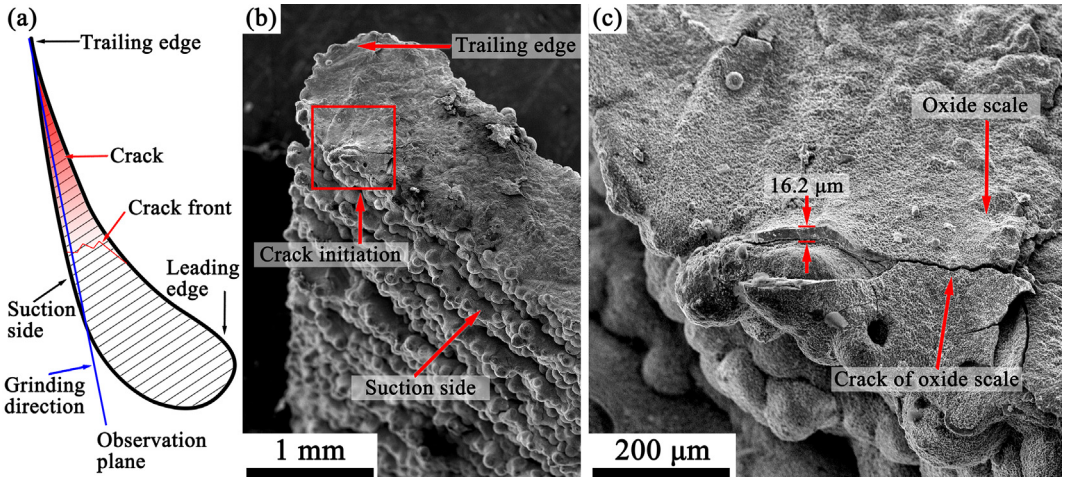

Fig. 4. SEM fractography: (a) schematic diagram of the sample examination after thermal shock experiment; (b) overall feature of the fracture surface; (c) high-magnification image showing crack initiation associated with the oxidation.

S6). We found that at the crack initiation region and along the crack path, oxides exhibited the local enrichment in Ti and Al, whereas only the Al enrichment can be seen near the crack tip. The duplex oxide characteristics can be further revealed by the three key observations. First, at the crack initiation region, the outer oxide layers were rich in Al and inner oxide layers were rich in Ti, suggesting Al_2O_3 was formed initially, followed by TiO_2. Second, along the crack propagation path (in the middle), the Ti enrichment found in the crack interior. Third, the EDS point analyses revealed location-specific Ti and Al variations s (Table S2). Thus, it can be deduced that at the early stage Al_2O_3 was formed, followed by the growth of a mixed Al_2O_3+TiO_2 scales, which occurred by breakdown of the initial Al_2O_3.

By using optimised SEBM process parameters (Table 1), the near-net-shape blades made of Ti-48Al-2Cr-2Nb has been fabricated (Fig. 1c). Due to the good process stability, the porosity level was controlled to be very low, helping to achieve the homogeneous microstructure. As a result, we successfully reduced the scatter in property (e.g. yield strength of 487.7±3.3 MPa at 700 °C). By comparison, the cast and hot-isostatic-pressed Ti-48Al-2Cr-2Nb alloy presented 344 MPa in the fully heat treated condition [28]. Along the radial direction of the blade, limited microstructural gradient was found, being consistent with the measured Al loss. The much finer lamellar colony size (from 8.3±4.5 μm to 9.7±6.0 μm along the Z-build) would help to reduce the micro-segregation. By comparison, the cast counterpart exhibits a value of 253±47 μm in [29], 232 to 283 μm in [28], and 200 to 400 μm in [30], which are much coarser than that as observed in the present work (Fig. 3).

Although no recommendations can be made at this stage for the development of oxidation resistant TiAl alloys tailored for

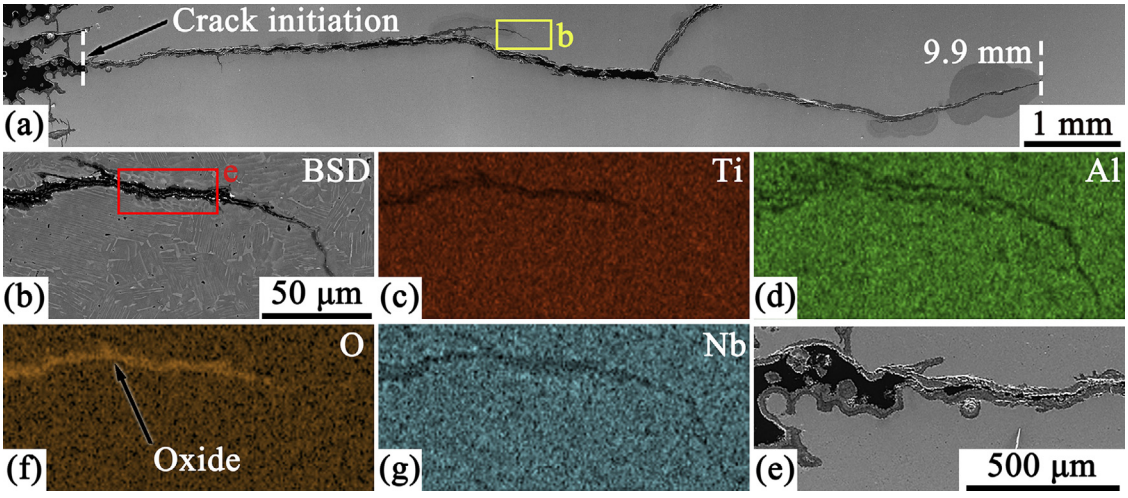

Fig. 5. SEM micrographs and corresponding EDS maps performed along the crack path: (a) the propagation path of a main crack; (b) to (g) EDS maps of Ti, Al, O and Nb along a selected crack with the crack tip included; (e) high-magnification SEM crack initiation area of the main crack. Note: additional SEM+EDS results can be found in Fig. S6.

SEBM process, alloying that helps to increase the stability of Al_2O_3 scale deserves future work. Moreover, the surface topology of as-fabricated blade via SEBM seems to play an important role in affecting the oxidation related thermal-shock failure at 900 °C (Fig. 5). Nevertheless, the Ti-48Al-2Cr-2Nb alloy is the current generation of γ-TiAl with operating temperatures of up to 700°C [15]. To this end, the SEBM-processed Ti-48Al-2Cr-2Nb blade meets the operating service requirement.

In summary, we showed that near-net-shape γ-TiAl blades can be processed reliably via SEBM, exhibiting a good combination of microstructure homogeneity, tensile properties and thermal shock resistance at 700 °C. Moreover, we unravelled a new crack mechanism under thermal shock at 900 °C, which appeared to be associated with the layerwise AM fabrication traces. We expect that the SEBM holds the promise of widening the γ-TiAl industrial applications as the manufacture cost and difficulties, microstructure inhomogeneity and associated large scatter in property can be reduced.

Declaration of Competing Interest

The authors declare that they have no known competing financial interests or personal relationships that could have appeared to influence the work reported in this paper.

Acknowledgement

Hui Peng acknowledges financial support from Key Areas Research and Development Program of Guangdong Province (Programme ID: 2018B090904004). Bo Chen acknowledges financial supports by the UK's Engineering and Physical Sciences Research Council, EPSRC First Grant Scheme EP/P025978/1 and Early Career Fellowship Scheme EP/R043973/1.

Supplementary materials

Supplementary material associated with this article can be found, in the online version, at doi:10.1016/j.scriptamat.2021.114092.

References

[1] H. Clemens, S. Mayer, Adv. Eng. Mater. 15 (2013) 191–215.
[2] T. Voisin, J.-P. Monchoux, M. Hantcherli, S. Mayer, H. Clemens, A. Couret, Acta Mater. 73 (2014) 107–115.
[3] D. Cormier, O. Harrysson, T. Mahale, H. West, Res. Lett. Mater. Sci. 34737 (2007) 1–4.
[4] L.E. Murr, S.M. Gaytan, A. Ceylan, E. Martinez, J.L. Martinez, D.H. Hernandez, B.I. Machado, D.A. Ramirez, F. Medina, S. Collins, R.B. Wicker, Acta Mater. 58 (2010) 1887–1894.
[5] J. Schwerdtfeger, C. Körner, Intermetallics 49 (2014) 29–35.
[6] S. Biamino, A. Penna, U. Ackelid, S. Sabbadini, O. Tassa, P. Fino, M. Pavese, P. Gennaro, C. Badini, Intermetallics 19 (2011) 776–781.
[7] M. Todai, T. Nakano, T. Liu, H.Y. Yasuda, K. Hagihara, K. Cho, M. Ueda, M. Takeyama, Addit. Manuf. 13 (2017) 61–70.
[8] W. Kan, B. Chen, H. Peng, Y. Liang, J. Lin, J. Alloys Compd. 809 (2019) 1–32.
[9] B. Gao, H. Peng, Y. Liang, J. Lin, B. Chen, Mater. Sci. Eng. A 811 (2021) 141059.
[10] J. Jin, R. Gao, H. Peng, H. Guo, S. Gong, B. Chen, Metall. Mater. Trans. A Phys. Metall. Mater. Sci. 51 (2020) 2411–2429.
[11] H. Gong, K. Rafi, H. Gu, T. Starr, B. Stucker, Addit. Manuf. 1 (2014) 87–98.
[12] J. Karlsson, T. Sjögren, A. Snis, H. Engqvist, J. Lausmaa, Mater. Sci. Eng. A 618 (2014) 456–461.
[13] S.H. Sun, Y. Koizumi, S. Kurosu, Y.P. Li, A. Chiba, Acta Mater. 86 (2015) 305–318.
[14] R. Pather, W.A. Mitten, P. Holdway, H.S. Ubhi, A. Wisbey, J.W. Brooks, Intermetallics 11 (2003) 1015–1027.
[15] Y.W. Kim, S.L. Kim, JOM 70 (2018) 553–560.
[16] A. Couret, J.P. Monchoux, D. Caillard, Acta Mater. 181 (2019) 331–341.
[17] A. Couret, D. Reyes, M. Thomas, N. Ratel-Ramond, C. Deshayes, J.P. Monchoux, Acta Mater. 199 (2020) 169–180.
[18] W. Kan, B. Chen, C. Jin, H. Peng, J. Lin, Mater. Des. 160 (2018) 611–623.
[19] A.J. Palomares-García, I. Sabirov, M.T. Pérez-Prado, J.M. Molina-Aldareguia, Scr. Mater. 139 (2017) 17–21.
[20] W. Kan, Y. Liang, H. Peng, B. Chen, H. Guo, J. Lin, JOM 69 (2017) 2596–2601.
[21] G. Sharma, R.V. Ramanujan, G.P. Tiwari, Acta Mater 48 (2000) 875–889.
[22] F. Qiang, H. Kou, L. Wang, J. Li, Mater. Charact. 167 (2020) 110474.
[23] J. Yang, B. Cao, Y. Wu, Z. Gao, R. Hu, Materialia 5 (2019) 100169.
[24] A.A. Antonysamy, J. Meyer, P.B. Prangnell, Mater. Charact. 84 (2013) 153–168.
[25] S. Becker, A. Rahmel, M. Schorr, M. Schutze, Oxid. Met. 38 (1992) 425–464.
[26] M.-X. Zhang, K.-C. Hsieh, J. DeKock, Y.A. Chang, Scr. Metall. Mater. 27 (1992) 1361–1366.
[27] A. Rahmel, M. Schütze, W.J. Quadakkers, Mater. Corros. 46 (1995) 271–285.
[28] Z. Gao, J. Yang, Y. Wu, R. Hu, S.L. Kim, Y.W. Kim, Metall. Mater. Trans. A 50 (2019) 5839–5852.
[29] C. Mercer, J. Lou, S.M. Allameh, W.O. Soboyejo, Metall. Mater. Trans. A 32 (2001) 2781–2794.
[30] M. Charpentier, D. Daloz, A. Hazotte, E. Gautier, G. Lesoult, M. Grange, Metall. Mater. Trans. A 34 A (2003) 2139–2148.